Localized high-concentration electrolytes get more localized through micelle-like structures

Corey M. Efaw [1,2,9], Qisheng Wu [3,9], Ningshengjie Gao [1], Yugang Zhang [4], Haoyu Zhu[2], Kevin Gering[1], Michael F. Hurley[2], Hui Xiong [2], Enyuan Hu [5], Xia Cao [6], Wu Xu [6], Ji-Guang Zhang [6], Eric J. Dufek [1], Jie Xiao [6,7], Xiao-Qing Yang [5], Jun Liu [6,7], Yue Qi [3] ✉ & Bin Li [1,2,8] ✉

Liquid electrolytes in batteries are typically treated as macroscopically homogeneous ionic transport media despite having a complex chemical composition and atomistic solvation structures, leaving a knowledge gap of the microstructural characteristics. Here, we reveal a unique micelle-like structure in a localized high-concentration electrolyte, in which the solvent acts as a surfactant between an insoluble salt in a diluent. The miscibility of the solvent with the diluent and simultaneous solubility of the salt results in a micelle-like structure with a smeared interface and an increased salt concentration at the centre of the salt–solvent clusters that extends the salt solubility. These intermingling miscibility effects have temperature dependencies, wherein a typical localized high-concentration electrolyte peaks in localized cluster salt concentration near room temperature and is used to form a stable solid–electrolyte interphase on a Li metal anode. These findings serve as a guide to predicting a stable ternary phase diagram and connecting the electrolyte microstructure with electrolyte formulation and formation protocols of solid–electrolyte interphases for enhanced battery cyclability.

Liquid electrolytes play a critical role in developing the high-energy rechargeable batteries needed to advance electric vehicle capabilities. Conventional low-concentration electrolytes (LCEs) need to be replaced to make long-life batteries a reality. The solvent-derived, instable and heterogeneous solid–electrolyte interphase (SEI) layers formed on high-capacity anodes, such as lithium (Li) metal, silicon (Si), sodium (Na) metal, zinc (Zn) metal and black phosphorus (BP), cannot accommodate large volume changes, leading to a continuous loss of active material and rapid dendrite growth.

One of the key pathways to harnessing highly reactive, yet energetic anodes is by regulating the electrolyte solvation structures beyond that of LCEs[1,2]. Increasing the salt concentration to form high-concentration electrolytes (HCEs) enables preferential anion reduction to form a stable, inorganic-rich SEI and reduce the parasitic reactions of free solvent molecules[3–7]. However, increasing salt concentration results in sluggish ion transport[5]. To mitigate this pitfall, a low viscosity diluent is added to form localized high-concentration electrolytes (LHCEs), thus improving the high-capacity anode performance

[1]Energy and Environmental Science and Technology Directorate, Idaho National Laboratory, Idaho Falls, ID, USA. [2]Micron School of Materials Science and Engineering, Boise State University, Boise, ID, USA. [3]School of Engineering, Brown University, Providence, RI, USA. [4]Center for Functional Nanomaterials, Brookhaven National Laboratory, Upton, NY, USA. [5]Chemistry Division, Brookhaven National Laboratory, Upton, NY, USA. [6]Energy and Environment Directorate, Pacific Northwest National Laboratory, Richland, WA, USA. [7]Materials Science and Engineering Department, University of Washington, Seattle, WA, USA. [8]Energy Science and Technology Directorate, Oak Ridge National Laboratory, Oak Ridge, TN, USA. [9]These authors contributed equally: Corey M. Efaw, Qisheng Wu. ✉e-mail: yueqi@brown.edu; lib2@ornl.gov
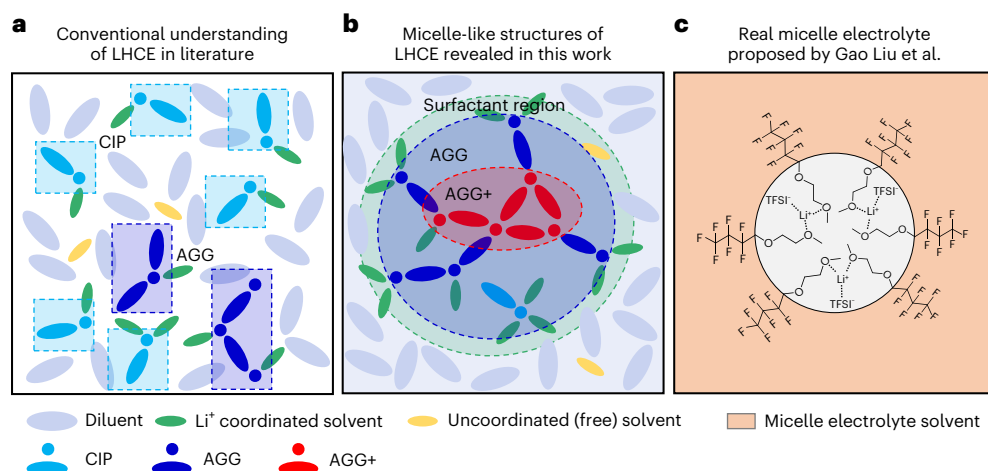
Fig. 1 | Schematics for the conventional understanding of LHCE, micelle-like structure of LHCE and real micelle electrolyte. a, Schematic for the conventional understanding of LHCE in the literature[7]. The light blue and purple areas refer to diluent and high-concentration salt–solvent clusters, respectively, where the clusters are maintained as they are in HCE. **b**, Schematic for the micelle-like structure of LHCE revealed in this work. **c**, The real micelle electrolyte (lithiophilic/phobic hydrofluoroether-based solvent in a LiTFSI–TTE electrolyte) proposed by Zhao et al., which is reproduced here from their work[25].

(for example, Li (refs. 8–11), Si (refs. 12,13), Na (ref. 14), Zn (refs. 15,16) and BP (refs. 17,18)).

Previous LHCE experiments and computations show that the cation solvation shells are fully occupied by the salt anion and solvent with minimal diluent participation[9,19]. Salt–solvent clusters of ~1 nm (ref. 20) are believed to retain a random, relatively uniform distribution (Fig. 1a), much like those in HCEs[7]. However, the information about LHCE microstructures, which bridges the size scales from atomistic solvation structures to macroscopically homogeneous liquid electrolyte, is still missing, leaving many unanswered questions. For example, why don't diluent molecules participate in the solvation shell[21,22]? Do the salt–solvent clusters agglomerate uniformly? Why does LHCE improve performance versus a HCE of the same salt-to-solvent molar ratio? In this paper, we propose a micelle-like structure in LHCE to unify the answers to these questions, by combining molecular dynamics (MD) simulations and Raman spectroscopy, along with small-angle and wide-angle X-ray scattering (SAXS–WAXS) for validation.

Analogous to the micelle concept for dispersed emulsions of non-mixing substances[23,24], the salt is insoluble in the diluent in a LHCE, while the diluent is miscible with the solvent[7]. A ternary phase diagram illustrates the interactions between salt, solvent and diluent and further demonstrates that the solvent acts as a surfactant, binding the immiscible salt and diluent phases, reducing the interfacial energy and stabilizing the dispersed liquid microstructure. The newly proposed micelle-like structure in LHCE (Fig. 1b) is based on the simulated structures of lithium bis(fluorosulfonyl)imide (LiFSI) salt, dimethoxyethane (DME) solvent and tris(2,2,2-trifluoroethyl)orthoformate (TFEO) diluent in coordination with analytical and electrochemical measurements. The solvent differs from traditional surfactant molecules, which typically have a polar-philic head and polar-phobic tail (for example, a hydrophilic/phobic water/oil emulsion[24] or lithiophilic/phobic hydrofluoroether-based solvent in a lithium bis(trifluoromethane) sulfonimide (LiTFSI)–1,1,2,2-tetrafluoroethyl-2,2,3,3-tetrafluoropropyl ether (TTE) electrolyte; Fig. 1c)[25]. For this reason, LHCE is referred to as 'micelle-like', where a network of salt–solvent clusters are mostly separated from the diluent matrix by a solvent-rich surfactant region (Fig. 1b). While this micelle-like structure is consistent with the previously proposed solvation structures of LHCEs[7], it further explains why those clusters are stable and improve upon their HCE counterparts.

The distribution of DME molecules is a result of minimizing the free energy of the ternary system. In addition to the interface region, a small fraction of DME exists in the miscible diluent matrix (Fig. 1b).

This explains the observation of increased free solvent molecules in the diluent with increasing diluent concentration[26]. DME in the matrix or near the interface region will naturally increase salt aggregation at the centre of the salt–solvent network. Figure 1b is idealized as a refined, circular network of clusters, while in reality it can be more complex in its shape and size[27].

Moreover, both salt–solvent and solvent–diluent interactions existing in the micelle-like structure are temperature sensitive, leading to a changing DME solvent distribution and local salt concentration with temperature. While many temperature- and rate-dependent SEI formation protocols have been proposed[28], detailed mechanisms are unclear. Here we demonstrate that the salt–solvent and solvent–diluent interactions impose different temperature dependencies. This is exemplified with a LHCE of LiFSI–1.2DME–2TFEO (where the numbers indicate mole ratios), where a local salt concentration peak at 25 °C is observed within the 10–45 °C temperature range, resulting in improved SEI composition and morphology, along with cycling performance. An additional LHCE formulation of LiFSI–dimethyl carbonate (DMC)–TTE was formulated to balance an improved micelle-like cluster network with macroscopic properties, resulting in an improved coulombic efficiency (CE) when compared to literature values. These findings suggest that controlling the underlying microstructure of a LHCE, through the optimization of the electrolyte component contributions and external parameters, directly impacts SEI design and battery optimization.

Micelle-like structure characteristics in LHCE

A ternary phase diagram and MD-simulated atomic structures of mixed LiFSI salt, DME solvent and TFEO diluent are provided in Fig. 2a. First, DME dissolves LiFSI up to a solubility limit (~1:1.05 LiFSI/DME by mole). Simulated HCEs (LiFSI–1.2DME and LiFSI–1.4DME) and LCE (LiFSI–9DME) are shown in Fig. 2b–d and Supplementary Fig. 1a–c. With Raman spectroscopy, the C–O stretching vibration modes of pure DME peaks (820–850 cm⁻¹) are reduced after LiFSI is dissolved in DME, blueshifting to 873–877 cm⁻¹ (ref. 29), corresponding to Li⁺ binding to ether oxygen atoms (Fig. 3a), as confirmed with MD simulations (Supplementary Fig. 2). DME and TFEO are miscible (Fig. 2e), while LiFSI has minimal or no solubility in TFEO, as confirmed by MD (Fig. 2f) and Raman analysis, where peaks are retained in the 820–870 cm⁻¹ range between TFEO and LHCE (Fig. 3a). Combining these component interactions reveals the solvent as a surfactant in LHCE, where TFEO has an almost-zero contribution to the Li⁺ solvation shell (Supplementary Fig. 1d,e), while DME exists mostly within the network of salt–solvent clusters with few
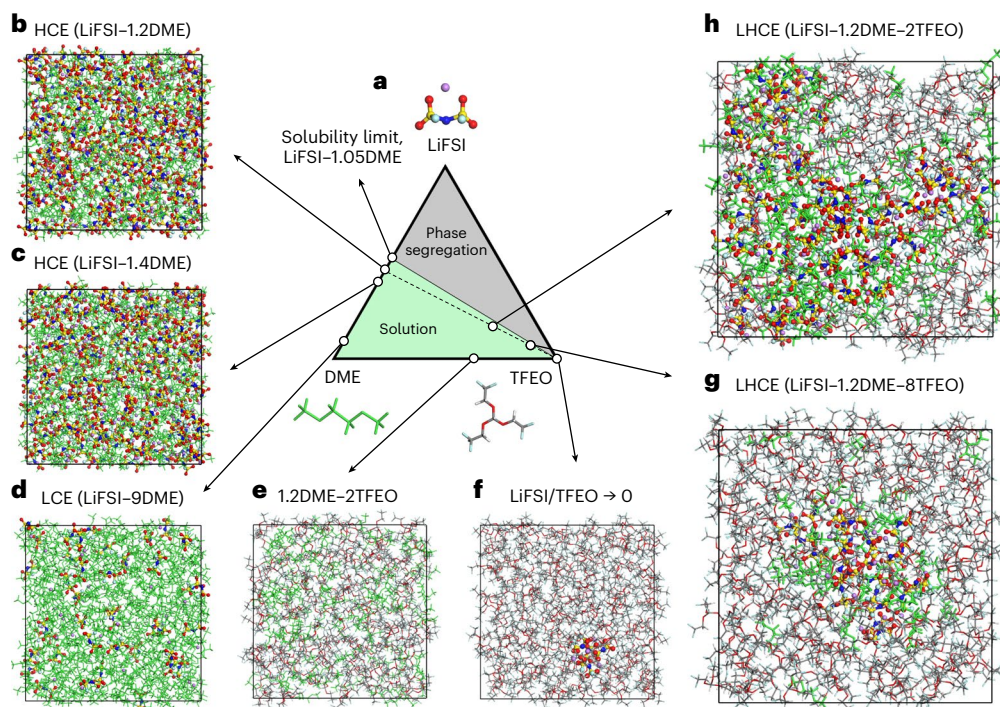
Fig. 2 | Ternary phase diagram of LiFSI salt, DME solvent and TFEO diluent.
a, Ternary phase diagram connecting the three variable phases: LiFSI, DME and
TFEO. The coloured ball-and-stick model shows LiFSI, while the green stick
model shows DME and the coloured stick model shows TFEO. The ternary phase
diagram is divided into two regions, the solution phase (green area) and the
phase segregation phase (that is, insoluble salt; grey area). **b,c**, MD-simulated
structures of HCE (LiFSI–1.2DME; **b**) and HCE (LiFSI–1.4DME; **c**), showing
uniformly distributed Li⁺–FSI⁻ clusters. The HCE (LiFSI–1.05DME) near the
solubility limit is also noted on the phase diagram. **d**, MD-simulated structure

of LCE (LiFSI–9DME), showing uniformly distributed Li⁺–FSI⁻ clusters. **e**, MD-
simulated structure of the mixed solvent and diluent (1.2DME–2TFEO), revealing
a high miscibility between the DME solvent and TFEO diluent. **f**, MD-simulated
structure of four LiFSI molecules in a TFEO matrix, revealing no solvation of the
LiFSI salt in TFEO. The cations and anions were initially and uniformly separated
in the TFEO diluent and formed the small cluster of 4 Li⁺ and 4 FSI⁻ by the end of
the simulation. **g,h**, MD-simulated structures of LHCE (LiFSI–1.2DME–8TFEO;
g) and LHCE (LiFSI–1.2DME–2TFEO; **h**), in both of which the network of salt–
solvent clusters is surrounded by a TFEO diluent matrix.

DME molecules in the TFEO matrix. The size and shape of the network
composed of salt–solvent clusters can vary when the ratios between
salt, solvent and diluent change (Fig. 2g,h).

The ability of solvents and diluents to solvate Li⁺ is thought to be
reflected by the dielectric constant and donor number[21], but this is
subject to debate. DME and TFEO have a similar dielectric constant
($\sim$7.0)[22,30] and similar binding energies to Li⁺ for single molecules
(2.81 eV versus 2.00 eV; Supplementary Fig. 3a,b). However, to form
a solvation shell, the number of solvating molecules depends on the
geometry of and the interaction with the solvated atom/molecule (for
example, four to five ethylene carbonate (EC) molecules[31], three DME
molecules or two TFEO molecules). When Li⁺ coordinates with three
DME molecules, the binding energy is comparable to a Li⁺–FSI⁻ ion
pair (5.39 eV versus 6.07 eV; Supplementary Fig. 3c,d). Li⁺ coordinat-
ing to two TFEO molecules exhibits a lower binding energy of 2.89 eV
(Supplementary Fig. 3e), driven by steric and electronic effects. Thus,
despite their comparable dielectric constants, DME solvates LiFSI
(Fig. 2b–d) while TFEO does not (Fig. 2f). As solubility reflects the inter-
actions between the binary systems, it serves as a stronger descriptor
than dielectric constant for LHCEs. Ultimately, the formation of the
micelle-like structure is maintained through a competition of energy of
mixing and interfacial interactions. The competition of these interac-
tions computed at the quantum level is carried into MD simulations to
ensure the accuracy of the liquid structures (Methods).

Higher local salt concentration in LHCE

The micelle-like structure pushes the local salt concentration in LHCE
higher than its HCE counterpart, which is validated by Raman spec-
troscopy. The Li⁺–FSI⁻ coordination strength is characterized by the

S–N–S symmetric stretching vibrational mode (715–780 cm⁻¹; Fig. 3a)[9].
Solid LiFSI salt ($\sim$775 cm⁻¹)[32] redshifts when dissolved in DME solvent,
driven by high sensitivity to Li⁺–FSI⁻ coulombic interactions[33]. The peak
further redshifts as salt concentration decreases, going from $\sim$753 cm⁻¹
near the solubility limit (LiFSI–1.05DME) to $\sim$749 cm⁻¹ for LiFSI–1.2DME,
$\sim$746 cm⁻¹ for LiFSI–1.4DME and $\sim$721 cm⁻¹ for LiFSI–9DME. Compa-
rably, LHCE (LiFSI–1.2DME–2TFEO) peaks at $\sim$752 cm⁻¹, blueshifting
from HCE with the same salt-to-solvent molar ratio (LiFSI–1.2DME),
suggesting a higher local salt concentration in LHCE. Furthermore,
Raman deconvolution analysis quantified the contributions of cluster
interactions. Following the literature[4,5,10], solvent-separated ion pairs
(SSIPs), contact ion pairs (CIPs), ion-pair aggregates (AGG) and more
coordinated ion-pair aggregates (AGG+) were defined by an increase
in anion–cation association (Fig. 3b)[33]. LCE is dominated by SSIP and
CIP, while HCEs and LHCE are prominently AGG and AGG+. Notably, the
ratio of AGG+ in LHCE (51.4%) is higher than that in its HCE counterpart
(40.4%), indicating a stronger Li⁺–FSI⁻ association.

In parallel, MD simulations and coordination analyses were
conducted. The salt–solvent clusters (SSIP, CIP, AGG and AGG+) are
categorized based on the FSI⁻–Li⁺ coordination number (CN; Sup-
plementary Fig. 4). As shown in Figs. 2h and 3c, LiFSI and DME form
a three-dimensional network of connected salt–solvent clusters sur-
rounded by a TFEO matrix. A salt concentration gradient is exhibited
within the salt–solvent clusters, where AGG+ tends to stay at the centre
of the network, while AGG resides nearer the outer shell (Fig. 3d), dif-
fering from the homogeneous spatial distributions of clusters in binary
electrolytes (Supplementary Fig. 5). Additionally, DME–Li⁺ interactions
accumulate at the interface between the cluster network and matrix,
playing the role of surfactant (Fig. 3c–e). Furthermore, a fraction of free
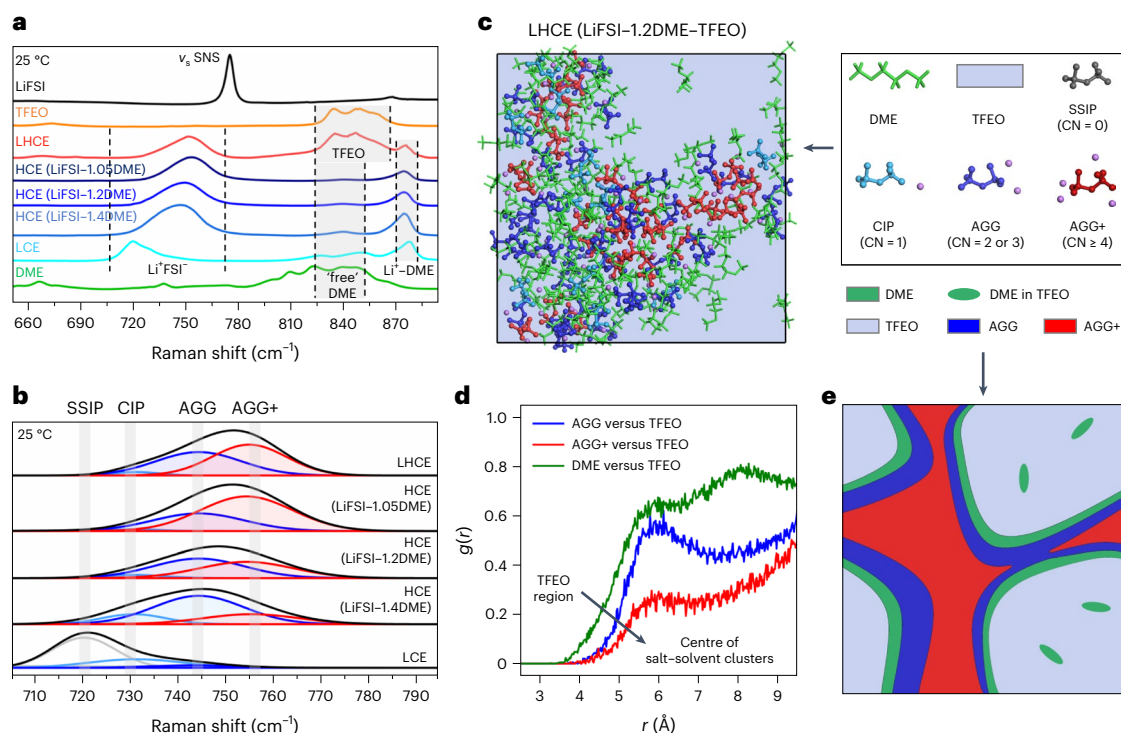
Fig. 3 | Raman spectroscopy and MD simulations of different systems at 25 °C. a, Raman spectra at 25 °C for (top to bottom) solid LiFSI crystal (black), TFEO (orange), LHCE (LiFSI–1.2DME–2TFEO, red), various HCEs (LiFSI–1.05DME as navy, LiFSI–1.2DME as blue and LiFSI–1.4DME as light blue), LCE (LiFSI–9DME, cyan) and DME (green). Different peak ranges are noted with dashed lines in the spectra. The v_s SNS indicates the S–N–S symmetric stretching vibrational mode. **b**, Deconvolution of Li⁺–FSI⁻ Raman peaks for LHCE, HCEs and LCE with peak fits for different cluster types denoted along the top. **c**, MD trajectory snapshot showing the spatial distributions of salt–solvent clusters in LHCE. The green stick model represents the DME molecule, the light blue area represents the TFEO matrix, the red ball-and-stick model indicates AGG+, the blue ball-and-stick model indicates AGG, the cyan ball-and-stick model indicates CIP and the dark grey ball-and-stick model indicates SSIP, while the black rectangular outline indicates the simulation boundary. **d**, Centre-of-mass radial distribution function (*g*) plots for the pairs of AGG versus TFEO, AGG+ versus TFEO and DME versus TFEO. Panels **c** and **d** show that AGG+ stays in the inner part of the network of salt–solvent clusters, while AGG and DME are mainly in the outer part. A fraction of DME molecules is completely dissolved into the TFEO matrix (that is, free DME). **e**, Schematic for the spatial distributions of DME, AGG and AGG+ in the LHCE. Green, blue and red areas indicate Li⁺-coordinated DME, AGG and AGG+ regions, respectively. The green ovals represent free DME molecules that are miscible in the light blue TFEO matrix.

DME molecules is completely dissolved in the miscible TFEO matrix (Fig. 3c,e), which further enhances the local salt concentration.

Evolution of micelle-like structure in LHCE

To provide insight into LHCE electrolyte design for further optimization, the factors to evolve the micelle-like structure are examined with a common LiFSI–1.2DME–2TFEO LHCE. A simple parameter that impacts salt–solvent solubility and solvent–diluent miscibility is temperature. The probability values of different salt–solvent clusters as a function of temperature (0, 10, 25, 45 and 60 °C) were obtained through Raman deconvolution (Supplementary Fig. 6a,b) and MD (Fig. 4a and Supplementary Fig. 6c,d), both indicating a local AGG+ ratio peak at 25 °C in the 10–45 °C temperature range (Supplementary Fig. 6b,d and Fig. 4b). MD shows lower AGG+/AGG ratios and more fluctuations, likely caused by smaller cluster sizes and limited cluster numbers; smaller clusters have a larger surface (that contains more AGG) to volume ratio. Regardless, two temperature-dependent solubility/miscibility effects are revealed. First, as temperature increases, more DME molecules migrate into the TFEO matrix (Fig. 4c). With fewer DME molecules coordinating with Li⁺, the anion–cation association increases inside the network of solvent–salt clusters. Second, DME dissolves more LiFSI as temperature increases, weakening the coordination strength between Li⁺ and FSI⁻ and causing the decomposition of higher-coordination aggregates, which is indirectly confirmed with binary HCEs (Fig. 4d and Supplementary Fig. 7). As a result, a 'Goldilocks phenomenon' for the ratio of AGG+ is observed when these two effects are intertwined

for the ternary LHCE. While the DME–TFEO miscibility effect is severe at extreme temperatures, it is mild in the 10–45 °C range, resulting in this Goldilocks phenomenon of a local AGG+/AGG ratio peak at 25 °C (Fig. 4b). The competition of salt–solvent solubility and solvent–diluent miscibility in the micelle-like LHCE can also be reflected by the effect of the diluent concentration. The AGG+ ratio increases with diluent concentration, caused by more DME molecules mixing into the TFEO matrix, which is validated through Raman analysis[9,10] (Supplementary Fig. 8) and MD (Supplementary Figs. 6d and 9). Raman results reveal a breakpoint to this effect, as an excess of TFEO results in a reduction in higher aggregate clusters.

Inspiring formation protocol for practical Li metal battery

Conventional wisdom limits battery operation to 10–45 °C, since a high temperature leads to extensive side reactions and rapid capacity fade, while a low temperature limits lithium utilization due to slow kinetics[34]. However, operating near extreme temperatures over a shortened time (for example, formation cycles) permits the formation of a more stable initial SEI while minimizing detrimental temperature-driven impacts.

To observe how salt–solvent clusters affect initial SEI formation and cyclability, formation cycles were run at 10 °C, 25 °C or 45 °C, followed by ageing cycles at 25 °C for LiFSI–1.2DME–2TFEO (Fig. 5a–c). The effects of temperature on overall cell capabilities are observed with the charge–discharge profiles during the first formation cycle, where lithium utilization (that is, discharge capacity) and initial
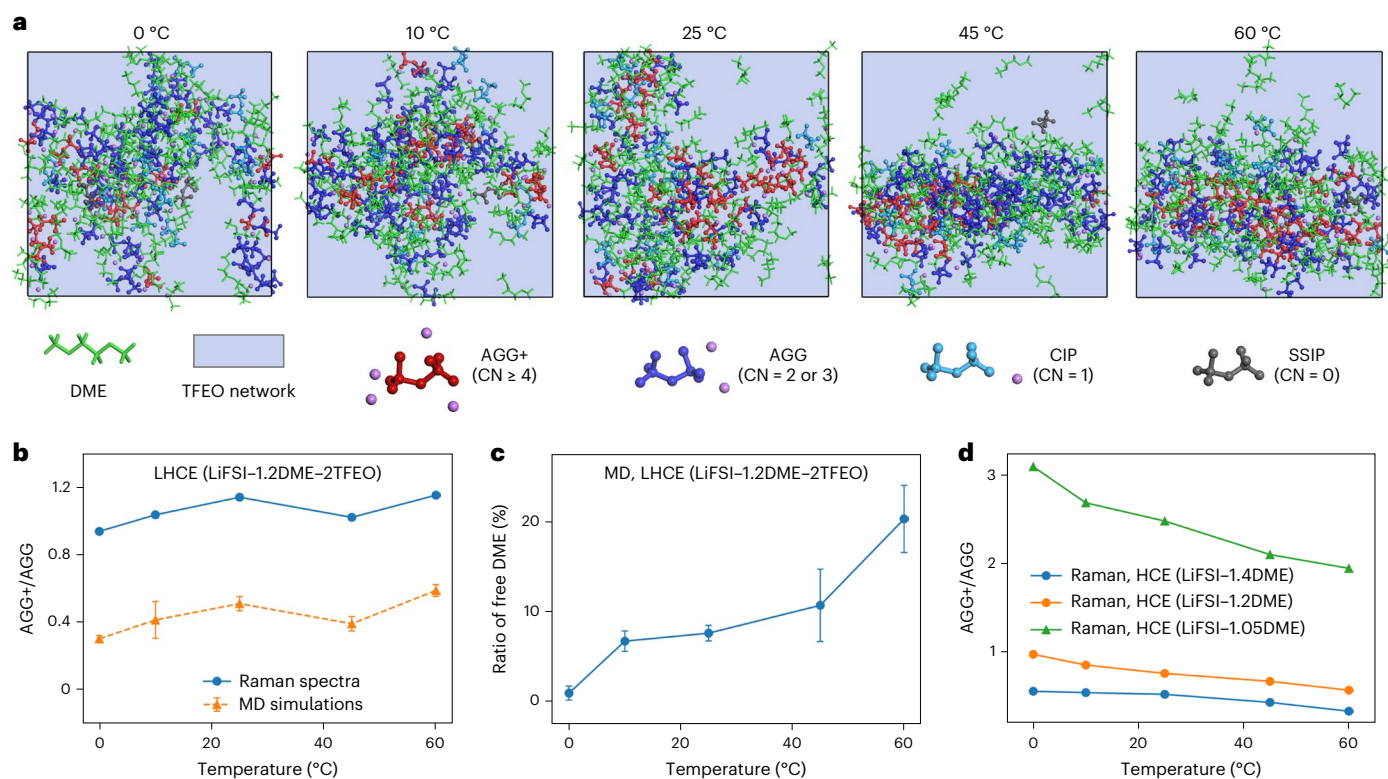
Fig. 4 | Raman spectroscopy and MD simulations of LHCE and HCEs at various temperatures. a, Snapshots taken from MD simulations showing the spatial distributions of the different cluster types (SSIP, CIP, AGG and AGG+) as well as DME molecules, at different temperatures. **b**, AGG+/AGG ratios as functions of temperature calculated through Raman analysis (solid blue line) and MD statistics (dashed orange line) for LHCE. **c**, Ratio of free DME molecules (that is, not coordinating with any Li^+) as a function of temperature for LHCE, calculated with MD. **d**, AGG+/AGG ratios as functions of temperature calculated

through Raman analysis for HCEs (LiFSI–1.4DME, LiFSI–1.2DME and LiFSI–1.05DME). All the reported values from MD simulations in **b** and **c** are averaged for a 4 ns production run, $\langle probability(4\ ns)\rangle$, with $n = 16,000$ (200 frames multiplying 80 LiFSI molecules). We define the error bar as the difference between the maximum and minimum in the time-averaged values, $error = \pm(\max\{\langle probability(t)\rangle\} - \min\{\langle probability(t)\rangle\})$, from time t of 2 ns to 4 ns during production runs.

overpotentials follow an Arrhenius temperature dependence (Fig. 5a)[34]. When equilibrated to 25 °C for ageing, discharge capacities and overpotentials are comparable (Fig. 5b), revealing that cell-level impacts are not substantial with the formation protocol at these different temperatures; rather, the primary impact of temperature is initial SEI formation driven by differences in LHCE microstructures. This is confirmed with cycle performance, where a 25 °C formation temperature outperformed 10 °C and 45 °C (Fig. 5c). This correlates to the increased AGG+ ratio at 25 °C (Fig. 4b) and thus an increase in salt-rendered SEI. Supplementary Fig. 10 shows that an increase in Li^+–FSI^- coordination increases the reduction potential, easing anion decomposition at the anode surface[8]. Although both MD simulations and Raman peak deconvolution analyses confirm that a greater AGG+/AGG ratio is shown at 60 °C (Fig. 4b), the extent of macroscale impacts (for example, extensive side reactions) would outweigh the benefit of improving electrolyte cluster statistics.

To confirm the impact of salt–solvent clusters on SEI formation, field emission scanning electron microscopy (FESEM) and X-ray photoelectron spectroscopy (XPS) with depth profiling were used to examine the surface morphology and composition, respectively, of discharged anodes after formation cycles. The SEI is thin at 25 °C when compared to other temperatures (Supplementary Fig. 11). Peak positioning as a function of sputter time reveals monolithic behaviour for 25 °C with a minimal transition in relative intensity (Fig. 5d–f). Additionally, there is minimal intensity in the organic carbon spectrum relative to inorganic components. For oxygen, the primary peak for 25 °C is Li_2O, whereas other temperatures are dominant in C–O and C=O, along

with transitions in relative peak intensities over sputter time[35]. Initial SEIs formed at 10 °C show more organic components than at 45 °C due to an increase in the probability of CIP structures (4.2% at 10 °C versus 2.5% at 45 °C; Supplementary Fig. 6b), driving poorer cycling performance. Hence, a relative reduction in organics versus inorganics (Supplementary Table 1) improves the initial SEI's chemical and mechanical stability. The formation of more inorganic SEI components would further suppress the decomposition of TFEO or DME (Supplementary Fig. 12). When examining FESEM results (Fig. 5g–i), metallic Li being stripped off at 10 °C and 45 °C resulted in non-uniform, porous surfaces, permitting active material consumption as cell operation continues. Comparatively, a stripped Li foil at 25 °C is uniform and compact, primarily driven by the increased monolithic and inorganic-rich SEI. Therefore, the primary impact that the chosen temperatures had during formation cycles was in the variation of salt–solvent clusters in the micelle-like LHCE, which can be used to predict the optimal formation cycle temperature.

Control of micelle-like structures for LHCE design

Conventional micelles form beyond a critical concentration of surfactant, the critical micelle concentration (CMC)[36], identified by conductivity trends[37,38]. Figure 6a shows the ionic conductivity of LiFSI–1.2DME–xTFEO with increasing LiFSI concentration, where the slope changes at a critical 'micelle-like' concentration ('CMC'), implying two different ionic conduction mechanisms. Below the 'CMC', ionic conductivity increases with ion concentration in the uniformly dispersed solution. Above the 'CMC', the ionic conductivity is mainly determined
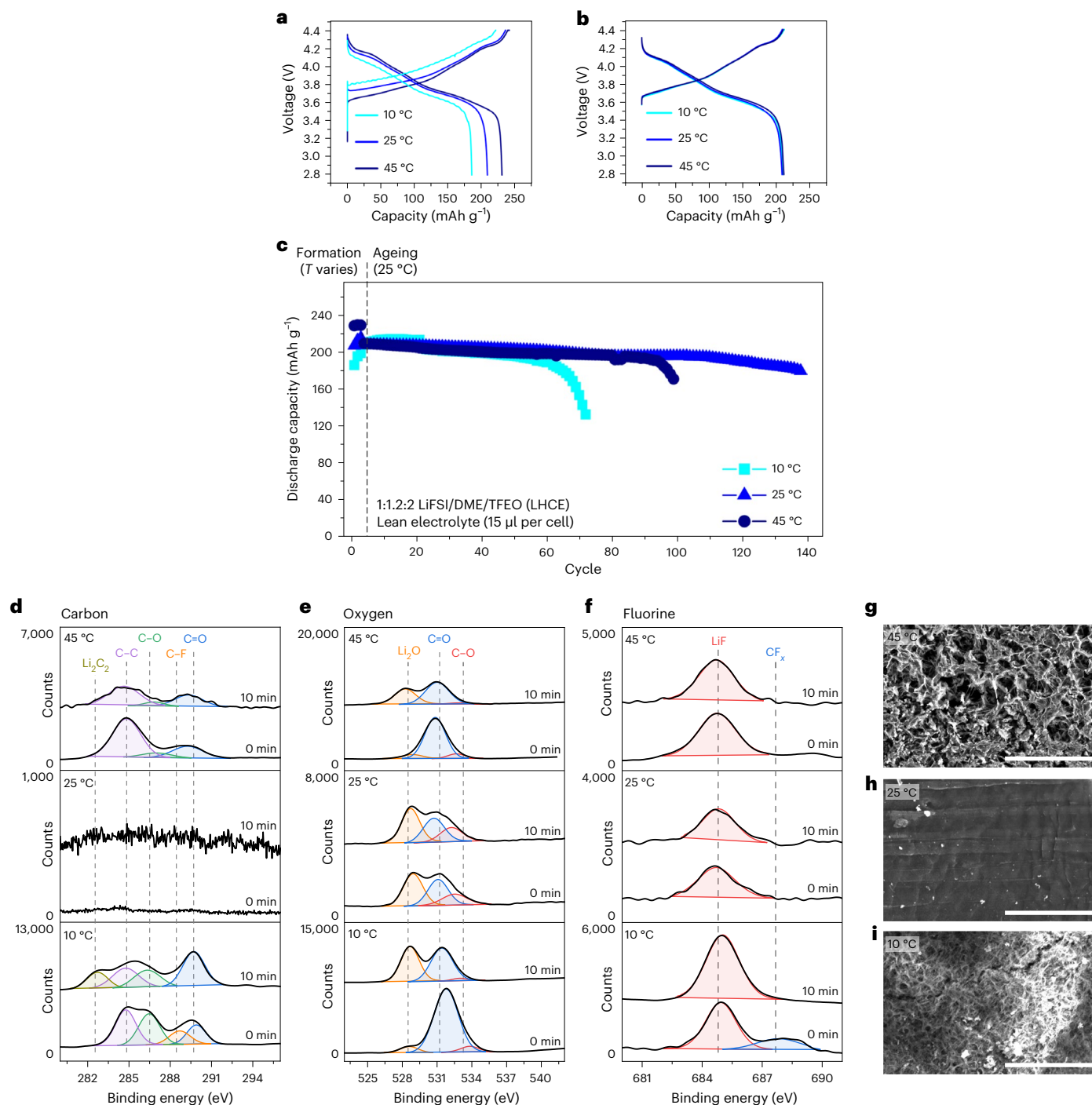
Fig. 5 | Electrochemical performances of LHCE-based cells at various formation temperatures and corresponding SEI components and morphologies. a, First formation cycle charge–discharge curves at several temperatures (*T* = 10, 25 and 45 °C). **b**, Second ageing cycle charge–discharge curves at 25 °C following formation cycling at several temperatures (10, 25 and 45 °C). **c**, Cycling performance at 25 °C for different formation protocols.

The dashed vertical line separates the period of formation from the period of ageing. **d**–**f**, Surface and depth analysis of delithiated lithium foils with XPS of carbon peaks (**d**), oxygen peaks (**e**) and fluorine peaks (**f**) after formation cycles at several temperatures (from bottom to top, 10, 25 and 45 °C). **g**–**i**, FESEM images (scale bars of 50 μm) of delithiated lithium foil surface morphologies after formation cycles at 45 °C (**g**), 25 °C (**h**) and 10 °C (**i**).

by the formation and connection of micelle-like structures. The 'CMC' is also identified in LiFSI–1.5DMC–*x*TTE (Supplementary Fig. 13).

Furthermore, the proposed micelle-like structures were identified by SAXS-WAXS (Fig. 6b). Electrolytes below the 'CMC' (*x* = 12 and 30) are comparable to the baseline (1.2DME–2TFEO), while electrolytes above the 'CMC' (*x* = 1 and 2) additionally peak at a wave vector transfer of $q \approx 0.135 \,\text{Å}^{-1}$ with a calculated diameter of ~47 Å ($2\pi/q$). The pair

distance distribution function, $P(r)$, shows an increasing peak in electrolytes above the 'CMC' with an estimated radius (r) of ~25 Å (Fig. 6c), suggesting the formation of micelle-like structures consistent with the results of Fig. 6a,b. Similarly, an increase in TFEO results in Li⁺–FSI⁻ red-shifting in Raman spectra (Supplementary Fig. 8; *x* = 12 and 30). As diluent concentration decreases, isolated micelles within the diluent matrix will connect into three-dimensional networks of salt–solvent clusters
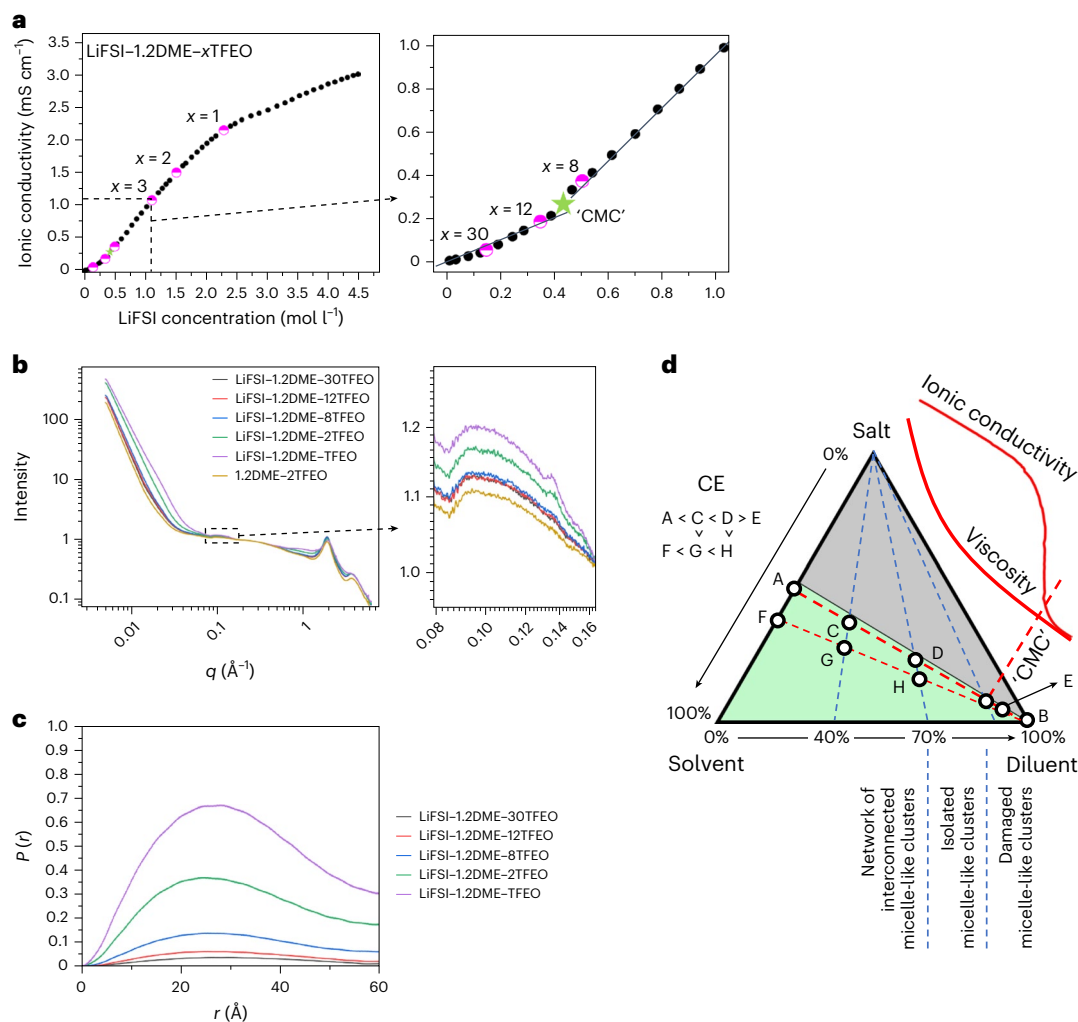
Fig. 6 | Features of micelle-like structures in LHCE and rational LHCE design. **a**, Ionic conductivities of LiFSI–1.2DME–xTFEO solutions as a function of LiFSI salt concentration, acquired between 21 °C and 22 °C. Specific solutions (pink circles), as well as the 'CMC' (in the zoomed-in inset as a green star) are noted. **b**, SAXS-WAXS patterns acquired at 25 °C with a small q range of LiFSI–1.2DME–xTFEO solutions (x = 1, 2, 8, 12 and 30) compared to 1.2DME–2TFEO co-solvent, as seen in the zoomed-in inset. **c**, Pair distance distribution function, $P(r)$, of LiFSI–1.2DME–xTFEO solutions (x = 1, 2, 8, 12 and 30) derived from SAXS patterns. **d**, Schematic showing LHCE design criteria according to ternary phase diagram. CE values are ranked for each position shown in the phase diagram. Ionic conductivity and viscosity (red) are exemplified along line A–B. 'CMC' is noted based on the ionic conductivity plot due to slope change.

(Fig. 2g,h). This is validated by the structure factor, $S(q)$, normalizing the SAXS data with respect to a dilute solution (Supplementary Fig. 14). Peak intensity increases with decreasing diluent concentration, suggesting more interactions among micelle-like structures. The results presented here unify multiple recent discussions on varying ionic transport mechanisms[39], ionic conductivity and aggregation structures with LHCE compositions[9,26]. While knowing the 'CMC' can guide the design of LHCEs, its structure and size depend on the chemistry and composition of the electrolyte, as well as external parameters (for example, temperature).

The ternary phase diagram (Fig. 6d) and the understanding of the micelle-like structures illustrate the proposed design criteria for a high-performance LHCE:

First, the concentration of diluent should be optimized by balancing macroscale properties (for example, viscosity and ionic conductivity) and microscale properties (for example, the size of the salt–solvent clusters and their connections in the micelle-like structures). In general, the continuous addition of diluent reduces viscosity versus HCEs[9,40,41] and leads to an increase in local salt concentration. The gradual increase in local salt concentration with diluent is driven by the formation of the micelle-like structures and 'CMC'. By increasing the amount of diluent

from point A to B (Fig. 6d), the local salt concentration first increases and then decreases (Supplementary Fig. 8), accompanied by transition points in the microstructure. Going from point C to point 'CMC', the micelle-like microstructure forms and evolves from an interconnected network (C–D) to isolated clusters (D–'CMC'; Fig. 2g,h). This coordinates with an increase in local salt concentration and reduction in ionic conductivity (Fig. 6a and Supplementary Fig. 13). Continuing beyond the 'CMC' (for example, point E), the micelle-like microstructure is damaged and reduces the local salt concentration. Therefore, comprehensively considering the microstructures and macroscale properties, the diluent accounts for 40–70% of all electrolyte species (salt, solvent and diluent) by mole (Fig. 6d), depending on the chemistries chosen (Supplementary Fig. 15a,b (ref. 9)).

Second, the electrolyte composition should be close to the 'solubility line' to extend local salt concentration. This supports increased AGG+ formation, which forms a salt-derived SEI, along with a higher CE value. In Fig. 6d, CE values at C and D should be higher than at G and H, respectively, due to the higher initial salt concentration in the equivalent solvent–diluent solutions. Including the knowledge of optimizing the concentration of diluent described in the first criterion mentioned above, CE values near D should be the highest due to

it having the highest local salt concentration and a viable micelle-like microstructure. These design criteria are well validated with the LiFSI–DME–TFEO system (Supplementary Fig. 15a) and LiFSI–DMC–TTE system (Supplementary Fig. 15b). For the LiFSI–DMC–TTE system, with the guidance shown in Fig. 6d, a CE above 99% was consistently achieved (Supplementary Figs. 15b and 16). Saturated LiFSI–1.5DMC–3.07TTE is instable over longer cycling, though it reaches a 99.59% CE for short-term Li || Cu testing. LiFSI–2.2DMC–4.5TTE, with the second highest CE of 99.54%, improves upon reported LHCE systems (Supplementary Table 2 and Supplementary Fig. 17).

Third, a salt/solvent system with higher salt solubility in solvents is preferred (Supplementary Fig. 15c)[42]. This is exemplified by an increase in initial lithium hexafluorophosphate (LiPF$_6$) salt concentration in EC/ethyl methyl carbonate (EMC; 1:2 by mole) compared to LiPF$_6$ in DME. Additionally, the salt solubility should differ slightly when operating temperature varies, ensuring the electrolyte formulation always lies close to the 'solubility line' in a wider temperature range. Understanding the necessary operation parameters and how they impact the micelle-like structures is paramount for a viable large-scale battery in varied conditions.

In summary, a ternary phase diagram for the design of LHCE is proposed based on salt–solvent solubility and solvent–diluent miscibility. Salt–solvent clusters in LHCE exhibit micelle-like behaviour. A salt concentration gradient naturally forms in a micelle-like cluster, through which the ion-pair aggregates get more localized due to the accumulation of solvent as a surfactant at the interfaces between the salt network and diluent matrix. The micelle-like structure is also influenced by the temperature. In an exemplary LHCE of LiFSI–1.2DME–2TFEO, a localized peak ratio of AGG+ is seen at 25 °C, confirmed with both Raman analysis and MD simulations; this result inspired a formation protocol that improved the initial SEI composition and morphology, and extended the cyclability. In the LiFSI–DMC–TTE system, a CE above 99.5% is accomplished, optimized by compensating microstructures (for example, micelle-like structures and network versus isolated clusters) with macroscale properties (for example, ionic conductivity). This work proposes methods of controlling the micelle-like structure in LHCE, supported by SAXS, Raman characterization and MD simulations, as well as electrochemical measurements, for higher performing practical batteries. From here, the impacts of electrolyte component choices in LHCEs to control the salt–solvent cluster size, shape and composition, as well as external parameters chosen during operation (for example, temperature), can be optimized to extend the anode stability and cyclability of high-energy batteries.

Online content

Any methods, additional references, Nature Portfolio reporting summaries, source data, extended data, supplementary information, acknowledgements, peer review information; details of author contributions and competing interests; and statements of data and code availability are available at https://doi.org/10.1038/s41563-023-01700-3.

References

1. Wang, Z. et al. Structural regulation chemistry of lithium ion solvation for lithium batteries. *EcoMat* **4**, e12200 (2022).
2. Cheng, H. et al. Emerging era of electrolyte solvation structure and interfacial model in batteries. *ACS Energy Lett.* **7**, 490–513 (2022).
3. Qian, J. et al. High rate and stable cycling of lithium metal anode. *Nat. Commun.* **6**, 6362 (2015).
4. Wang, J. et al. Superconcentrated electrolytes for a high-voltage lithium-ion battery. *Nat. Commun.* **7**, 12032 (2016).
5. Yamada, Y. & Yamada, A. Review—superconcentrated electrolytes for lithium batteries. *J. Electrochem. Soc.* **162**, A2406–A2423 (2015).
6. Suo, L., Hu, Y. S., Li, H., Armand, M. & Chen, L. A new class of solvent-in-salt electrolyte for high-energy rechargeable metallic lithium batteries. *Nat. Commun.* **4**, 1481 (2013).
7. Cao, X., Jia, H., Xu, W. & Zhang, J.-G. Review—localized high-concentration electrolytes for lithium batteries. *J. Electrochem. Soc.* **168**, 010522–010522 (2021).
8. Cao, X. et al. Monolithic solid-electrolyte interphases formed in fluorinated orthoformate-based electrolytes minimize Li depletion and pulverization. *Nat. Energy* **4**, 796–805 (2019).
9. Cao, X. et al. Optimization of fluorinated orthoformate based electrolytes for practical high-voltage lithium metal batteries. *Energy Storage Mater.* **34**, 76–84 (2021).
10. Li, T. et al. Stable anion-derived solid electrolyte interphase in lithium metal batteries. *Angew. Chem. Int Ed.* **60**, 22683–22687 (2021).
11. Adams, B. D., Zheng, J. M., Ren, X. D., Xu, W. & Zhang, J. G. Accurate determination of coulombic efficiency for lithium metal anodes and lithium metal batteries. *Adv. Energy Mater.* **8**, 1702097 (2018).
12. Jia, H. P. et al. Controlling ion coordination structure and diffusion kinetics for optimized electrode-electrolyte interphases and high-performance Si anodes. *Chem. Mater.* **32**, 8956–8964 (2020).
13. Peng, X. D., Lin, Y. K., Wang, Y., Li, Y. J. & Zhao, T. S. A lightweight localized high-concentration ether electrolyte for high-voltage Li-ion and Li-metal batteries. *Nano Energy* **96**, 107102 (2022).
14. Wang, Y. D. et al. Enhanced sodium metal/electrolyte interface by a localized high-concentration electrolyte for sodium metal batteries: first-principles calculations and experimental studies. *ACS Appl. Energy Mater.* **4**, 7376–7384 (2021).
15. Wang, N. et al. Stabilized rechargeable aqueous zinc batteries using ethylene glycol as water blocker. *ChemSusChem* **13**, 5556–5564 (2020).
16. Xue, R. F. et al. Highly reversible zinc metal anodes enabled by a three-dimensional silver host for aqueous batteries. *J. Mater. Chem. A* **10**, 10043–10050 (2022).
17. Du, X. Q. & Zhang, B. A. Robust solid electrolyte interphases in localized high concentration electrolytes boosting black phosphorus anode for potassium-ion batteries. *ACS Nano* **15**, 16851–16860 (2021).
18. Qin, L. et al. Pursuing graphite-based K-ion O$_2$ batteries: a lesson from Li-ion batteries. *Energy Environ. Sci.* **13**, 3656–3662 (2020).
19. Piao, N. et al. Countersolvent electrolytes for lithium-metal batteries. *Adv. Energy Mater.* **10**, 1903568 (2020).
20. Qian, K., Winans, R. E. & Li, T. Insights into the nanostructure, solvation, and dynamics of liquid electrolytes through small-angle X-ray scattering. *Adv. Energy Mater.* **11**, 2002821 (2021).
21. Su, C. C. et al. Solvating power series of electrolyte solvents for lithium batteries. *Energy Environ. Sci.* **12**, 1249–1254 (2019).
22. Cao, X., Zhang, J.-G. & Xu, W. Electrolyte for stable cycling of rechargeable alkali metal and alkali ion batteries. US patent: US20200161706A1 (2019).
23. McBain, J. W. Mobility of highly-charged micelles. *Trans. Faraday Soc.* (1913).
24. McClements, D. J. Nanoemulsions versus microemulsions: terminology, differences, and similarities. *Soft Matter* **8**, 1719–1729 (2012).
25. Zhao, Y. et al. A micelle electrolyte enabled by fluorinated ether additives for polysulfide suppression and Li metal stabilization in Li-S battery. *Front. Chem.* https://doi.org/10.3389/fchem.2020.00484 (2020).
26. Ren, F. et al. Solvent–diluent interaction-mediated solvation structure of localized high-concentration electrolytes. *ACS Appl. Mater. Interfaces* **14**, 4211–4219 (2022).

27. Beltran, S. P., Cao, X., Zhang, J. G. & Balbuena, P. B. Localized high concentration electrolytes for high voltage lithium-metal batteries: correlation between the electrolyte composition and its reductive/oxidative stability. *Chem. Mater.* **32**, 5973–5984 (2020).

28. Genovese, M. et al. Hot formation for improved low temperature cycling of anode-free lithium metal batteries. *J. Electrochem. Soc.* **166**, A3342–A3347 (2019).

29. Yoshida, H. & Matsuura, H. Density functional study of the conformations and vibrations of 1,2-dimethoxyethane. *J. Phys. Chem. A* **102**, 2691–2699 (1998).

30. Cote, J. F. et al. Dielectric constants of acetonitrile, gamma-butyrolactone, propylene carbonate, and 1,2-dimethoxyethane as a function of pressure and temperature. *J. Solut. Chem.* **25**, 1163–1173 (1996).

31. Pham, T. A., Kweon, K. E., Samanta, A., Lordi, V. & Pask, E. J. Solvation and dynamics of sodium and potassium in ethylene carbonate from ab initio molecular dynamics simulations. *J. Phys. Chem. C* **121** 21913–21920 (2017).

32. Kerner, M., Plylahan, N., Scheers, J. & Johansson, P. Thermal stability and decomposition of lithium bis(fluorosulfonyl)imide (LiFSI) salts. *RSC Adv.* **6**, 23327–23334 (2016).

33. Suo, L., Zheng, F., Hu, Y. S. & Chen, L. FT-Raman spectroscopy study of solvent-in-salt electrolytes. *Chin. Phys. B* **25**, 016101 (2015).

34. Wang, J. et al. Improving cyclability of Li metal batteries at elevated temperatures and its origin revealed by cryo-electron microscopy. *Nat. Energy* **4**, 664–670 (2019).

35. Sun, B. et al. At the polymer electrolyte interfaces: the role of the polymer host in interphase layer formation in Li-batteries. *J. Mater. Chem. A* **3**, 13994–14000 (2015).

36. Nagarajan, R. in *Structure-Performance Relationships in Surfactants* (eds Esumi, K. & Ueno, M.) 1–89 (Marcel Dekker, 2003).

37. Pal, A. & Chaudhary, S. Ionic liquids effect on critical micelle concentration of SDS: conductivity, fluorescence and NMR studies. *Fluid Phase Equilib.* **372**, 100–104 (2014).

38. Perez-Rodriguez, M. et al. A comparative study of the determination of the critical micelle concentration by conductivity and dielectric constant measurements. *Langmuir* **14**, 4422–4426 (1998).

39. Yamada, Y., Wang, J., Ko, S., Watanabe, E. & Yamada, A. Advances and issues in developing salt-concentrated battery electrolytes. *Nat. Energy* **4**, 269–280 (2019).

40. Chen, S. R. et al. High-efficiency lithium metal batteries with fire-retardant electrolytes. *Joule* **2**, 1548–1558 (2018).

41. Ren, X. D. et al. Localized high-concentration sulfone electrolytes for high-efficiency lithium-metal batteries. *Chem* **4**, 1877–1892 (2018).

42. Su, L. S. et al. Uncovering the solvation structure of LiPF$_6$-based localized saturated electrolytes and their effect on LiNiO$_2$-based lithium-metal batteries. *Adv. Energy Mater.* **12**, 2201911 (2022).

Methods

Materials synthesis

Lithium foil (50 µm, China Energy Lithium) was punched into ~1.43-cm-diameter discs and rolled onto stainless steel spacers. A $LiNi_{0.8}Mn_{0.1}Co_{0.1}O_2$ (NMC811) cathode coated on aluminium foil (Pacific Northwest National Lab, PNNL) was stored in a glove box and punched into 1.27-cm-diameter discs. NMC811 has a practical capacity of 4.34 mAh cm^{-2}. Celgard 2325, cut at ~1.59 cm diameter, was used as a separator. Different ether-based electrolytes were formulated and labelled as follows: LCE was a 1:9 molar ratio of LiFSI (Nippon Shokubai) in DME (Sigma-Aldrich); HCE was various molar ratios of LiFSI in DME (1:1.4, 1:1.2, 1:1.05); and LHCE incorporated diluent TFEO (SynQuest Laboratories) in 1:1.2:x LiFSI/DME/TFEO molar ratios (x = 1, 2, 8, 12 and 30). Prior to coin cell assembly, the CR2032 components, spacers and spring (MTI) were ultrasonicated in ethanol for 15 minutes, followed by deionized water for 15 minutes. Materials were then dried at 60 °C under vacuum below −75 kPa for at least 8 hours and held under vacuum in the argon-filled glove box antechamber for at least 8 hours prior to loading into the glove box. Aluminium cladded foil and a positive-side case were used on the cathode side to reduce LiFSI corrosion to the stainless-steel positive case.

Electrochemical measurements

All electrochemical experiments were done with CR2032-type cells (MTI). Galvanostatic cycling of Li ∥ NMC811 or Cu ∥ NMC811 full cells was done in an operating window between 2.8 and 4.4 V with C/10 charge and discharge rates for three formation cycles in environmental chambers set at 10 °C, 25 °C or 45 °C, where 1 C = 4.34 mA cm^{-2}. Some 15 µl of electrolyte was loaded into each cell. Cells were rested for 1 hour between each charge and discharge half cycle. Upon completion of the formation cycles, cells were placed into a 25 °C chamber and left at rest for 12 hours to allow thermal equilibration. Ageing cycles at C/10 charge and C/5 discharge rates were then run at 25 °C regardless of formation cycle temperature, with 15 minutes of rest between charge and discharge half cycles. The ionic conductivity of the electrolyte was measured in a glove box at room temperature with a model CM-30R conductivity meter (DKK-TOA).

CE tests are described elsewhere and used the modified Aurbach's method protocol, 'Method 3' (ref. 11), with a formation capacity (Q_T) of 5 mAh cm^{-2}, cycling capacity (Q_C) of 1 mAh cm^{-2}, cycling rate of 0.5 mA cm^{-2} and number of cycles (n) of 10 (ref. 11). Li ∥ Cu cells were assembled inside an argon-filled glove box (MBraun; H_2O < 1 ppm, O_2 < 1 ppm). Some 75 µl of electrolyte was added to each cell.

Characterization

Raman analysis was conducted by placing the solution (or solid salt) on a concave microscope slide (W. W. Grainger), and then sealing the slide with optical adhesive and a fused silica disc (Edmund Optics). The samples were exposed to various temperatures of 0 °C, 10 °C, 25 °C, 45 °C and 60 °C for Raman measurements. Raman spectroscopy was accomplished using a Horiba LabRAM HR Evolution (Horiba Scientific) equipped with a 50 mW monochromatic 532 nm doubled neodymium-doped yttrium aluminum garnet (Nd:YAG) laser with ~0.3 cm^{-1} spectral resolution. The spatial resolution, with a ×20 lens magnification, was between 0.5 and 1 µm. Spectra were processed with LabSpec v.6.3.x (Horiba Scientific). Spectra underwent a baseline correction and the denoising process to remove broadening and background noise, respectively. Gauss peak fitting with a zeroed y offset was used to deconvolute peaks of interest from spectra with ≥0.98 R^2 (coefficient of determination) regression. The area of each fitted peak was used to compare different peak contributions.

Post-mortem analysis of lithium foils was done after formation cycles at 10 °C, 25 °C and 45 °C. Cells were decrimped after cycling, followed by electrode rinsing with DME, and were dried in vacuum prior to analysis. XPS with a 1,253.6 eV Mg (Kα) X-ray source was used

to provide surface analysis with a PHI-5600 (Physical Electronics), along with an Ar$^+$ ion gun (2 kV, 1.2 µA) for sputter depth profiling. Sample charging was neutralized with a low-energy electron gun. A vacuum transfer vessel (PHI Model 04-110) was used to prevent air exposure. Peak position calibration is referenced to adventitious C 1s, the C–C peak at 284.8 eV, or to LiF at 684.7 eV if there was limited carbon present. PHI MultiPak software (Physical Electronics) was used with a mixed Gauss–Lorentzian peak fitting with >80% Gauss for each XPS peak. A FEI Teneo FESEM instrument was used to observe surface morphology. Brief air exposure (<1 minute) occurred when transferring electrodes into the FESEM chamber.

The SAXS and WAXS measurements were conducted at the Soft Matter Interfaces beamline (12-ID) of the National Synchrotron Light Source II (NSLS-II) at Brookhaven National Laboratory. The liquid samples were loaded into Kapton capillaries with a diameter of 1.5 mm, which were then sealed well and mounted on the Soft Matter Interfaces beamline sample stage. The scattered data were collected using a beam energy of 16.1 keV and beam size of 200 µm × 30 µm. A Pilatus 1M area detector (Dectris) was used for SAXS. The detector, consisting of 0.172 mm square pixels in a 981 × 1,043 array, was placed five metres downstream from the sample position. The WAXS data were collected with a PILATUS3 900 kW detector (Dectris), consisting of 0.172 mm square pixels in a 1,475 × 619 array. To obtain a wide range of wave vector transfer values (q), a series of two-dimensional diffraction patterns was collected by rotating the WAXS detector on an arc, with the sample-to-detector distance being 275 mm. Scattering patterns from each detector angle were stitched together using home-developed software. Then, both SAXS and WAXS two-dimensional scattering patterns were reduced to a one-dimensional scattering intensity, $I(q)$, by circular average. The q is the wave vector transfer, $q = (4\pi/\lambda)\sin(\theta)$, where $\lambda = 0.77$ Å and 2θ are the wavelength of the incident X-ray beam and the scattering angle, respectively.

MD simulations

All MD simulations were conducted using the Forcite module in Materials Studio 2020 (ref. 43). The COMPASS III force field was used along with optimized atom types and charges, which were all taken from previous works[44], except for the fact that the charges of Li$^+$ and FSI$^-$ from the salts are scaled by 0.7 to properly account for the ion–ion and ion–dipole interactions. The representative atom types and charges are shown in Supplementary Fig. 18. In terms of the interactions between the cation with the anion, the solvent and the diluent, as well as the density, ion conductivity, Li$^+$ coordination, ion pairing and aggregation ratios in both the high- and low-concentration electrolytes, the scaling factor of 0.7 gave either similar or better results (closer agreement with experiments[3,45] and/or simulation results based on polarizable force field[3,46] or density functional theory[47]) when compared with the scaling factor of 0.8, as discussed in our previous publication[48] and in the Supplementary Information (Supplementary Figs. 19 and 20 and Supplementary Tables 3–6). In particular, switching the scaling factor from 0.8 to 0.7 would result in a decrease in FSI$^-$ coordination with Li$^+$ (through its O atoms) by almost 1 in 1 M LiFSI–9DME electrolyte. The difference is much less for LiPF$_6$ pairs in EC–EMC mixed solvents. As cation–anion coordination is critical for solvation structures, it requires careful tests or using the systematic Molecular Dynamics Electronic Continuum (MDEC) model[49,50], which gave an optimal scaling factor (0.73) for LiFSI in DME.

It is challenging to obtain equilibrium heterogeneous liquid structures in LHCE. We approached this by considering different initial structures: (1) immersing a LiFSI salt cluster in mixed solvent/diluent; (2) comparing salt–solvent clusters at different sizes in TFEO diluent; and (3) randomly mixing/packing all species (LiFSI, DME and TFEO) through the Amorphous module in Materials Studio 2020 (ref. 43). After 20 ns dynamics, the initial structures with salt–solvent clusters (2) showed lower energy than (1) and (3), and the initial structure

with the lowest average energy was used to mimic the LHCE structure (Supplementary Fig. 21).

The electrolyte systems (Supplementary Table 7) were subjected to three stages of constant number, pressure and temperature (*NPT*) simulations, including a 2.0 ns pre-equilibrium run at room temperature, a long equilibrium run at a desired temperatures (0 °C, 10 °C, 25 °C, 45 °C and 60 °C) and a 4 ns production run to obtain statistics. The LHCEs (LiFSI–1.2DME–2TFEO and LiFSI–1.2DME–8TFEO) require a longer equilibrium run of 16.0 ns, compared to the 4 ns equilibrium run that is needed for HCEs (LiFSI–1.4DME and LiFSI–1.2DME) and LCE (LiFSI–9DME). The Nose–Hoover method[51] and Berendsen method[52] were used to control the temperature and pressure, respectively. For the LiFSI crystal simulations, equilibrium runs were performed for 1.0 ns followed by production runs for 1.0 ns at 25 °C. For both the LiFSI–TFEO and DME–TFEO mixture systems, the *NPT* simulations were conducted for 22.0 ns at 25 °C.

MD-based CN analyses

The statistics of the CN and the subsequent categorized aggregate ratios were analysed through our home-made perl and Python scripts, which are available upon request (Supplementary Figs. 21–25). Through the time evolution CN(t), the time-averaged $\langle \mathrm{CN}(t) \rangle$ from the beginning of the production run to time t was calculated. All the reported values are averaged for a 4 ns production run, $\langle \mathrm{CN}(4\,\mathrm{ns}) \rangle$. We defined the error bar as the difference between the maximum and minimum in the time-averaged values, error $= \pm(\max\{\langle \mathrm{CN}(t) \rangle\} - \min\{\langle \mathrm{CN}(t) \rangle\})$, from 2 ns to 4 ns during production runs (Supplementary Figs. 23–26 for time evolution and running averages of CN and ratios of aggregates). The error bars are generally small in homogeneous LCE and HCE and become larger in heterogeneous LCHE. Thus, we run additional 10 ns *NPT* dynamics for LHCE for further validation (Supplementary Fig. 27). The conclusion holds, considering the error bar, including the occurrence of a peak value of AGG+/AGG at room temperature, which shows larger scattering. This is likely due to the smaller cluster sizes in MD simulations compared to experiments. In our CN analyses, FSI$^-$ (or DME, TFEO) and Li$^+$ are considered as coordinated with each other if the Li$^+$ ion falls within 2.8 Å of any of the O, N and F atoms in the FSI$^-$ anion (or DME, TFEO). The radial distribution function plots (Supplementary Fig. 1) show that the value of 2.8 Å is close to the first minimum after the primary peak (~3.0 Å), which is often considered as the first coordination shell in the literature[53]. Our analyses show that the same trends can be obtained in terms of the ratios of the salt–solvent clusters (SSIP, CIP, AGG and AGG+) when using other cut-off values (2.4 Å or 3.2 Å), as shown in Supplementary Fig. 28. A DME molecule in LHCE is considered as free DME when it is not coordinating with Li$^+$ ions (that is, none of its ether oxygen atoms are within 2.8 Å of any Li$^+$).

Density functional theory calculations

All density functional theory calculations were conducted using the Gaussian 09 code[54]. The double hybrid functional M06-2X (ref. 55) and the basis set 6–31 + G** along with the D3 dispersion correction[56] were used. The implicit SMD model[57] and the dielectric constant of 7.2 were used to account for the solvation environment when calculating the reduction and oxidation potentials.

Data availability

The authors declare that all data supporting the findings of this study are included within the paper and its Supplementary Information. Source data are available from the corresponding authors (B.L. and Y.Q.) upon reasonable request.

Code availability

The Python scripts that have been used for MD analyses are available from the corresponding author (Y.Q.) upon request.

References

43. Materials Studio 2020 (Dassault Systèmes BIOVIA, 2020).
44. Akkermans, R. L. C., Spenley, N. A. & Robertson, S. COMPASS III: automated fitting workflows and extension to ionic liquids. *Mol. Simula.* **47**, 540–551 (2021).
45. von Cresce, A. & Xu, K. Preferential solvation of Li$^+$ directs formation of interphase on graphitic anode. *Electrochem. Solid St.* **14**, A154–A156 (2011).
46. Borodin, O. & Smith, G. D. Quantum chemistry and molecular dynamics simulation study of dimethyl carbonate: ethylene carbonate electrolytes doped with LiPF$_6$. *J. Phys. Chem. B* **113**, 1763–1776 (2009).
47. Borodin, O. et al. Competitive lithium solvation of linear and cyclic carbonates from quantum chemistry. *Phys. Chem. Chem. Phys.* **18**, 164–175 (2016).
48. Wu, Q. S., McDowell, M. T. & Qi, Y. Effect of the electric double layer (EDL) in multicomponent electrolyte reduction and solid electrolyte interphase (SEI) formation in lithium batteries. *J. Am. Chem. Soc.* **145**, 2473–2484 (2023).
49. Liu, H. et al. Ultrahigh coulombic efficiency electrolyte enables Li‖SPAN batteries with superior cycling performance. *Mater. Today* **42**, 17–28 (2021).
50. Park, C. et al. Molecular simulations of electrolyte structure and dynamics in lithium–sulfur battery solvents. *J. Power Sources* **373**, 70–78 (2018).
51. Nose, S. A unified formulation of the constant temperature molecular-dynamics methods. *J. Chem. Phys.* **81**, 511–519 (1984).
52. Berendsen, H. J. C., Postma, J. P. M., van Gunsteren, W. F., DiNola, A. & Haak, J. R. Molecular dynamics with coupling to an external bath. *J. Chem. Phys.* **81**, 3684–3690 (1984).
53. Toxvaerd, S. & Dyre, J. C. Role of the first coordination shell in determining the equilibrium structure and dynamics of simple liquids. *J. Chem. Phys.* **135**, 134501–134501 (2011).
54. Gaussian 09, revision D.01 (Gaussian, Inc., 2016).
55. Zhao, Y. & Truhlar, D. G. The M06 suite of density functionals for main group thermochemistry, thermochemical kinetics, noncovalent interactions, excited states, and transition elements: two new functionals and systematic testing of four M06-class functionals and 12 other functionals. *Theor. Chem. Acc.* **120**, 215–241 (2008).
56. Grimme, S., Ehrlich, S. & Goerigk, L. Effect of the damping function in dispersion corrected density functional theory. *J. Comput. Chem.* **32**, 1456–1465 (2011).
57. Marenich, A. V., Cramer, C. J. & Truhlar, D. G. Universal solvation model based on the generalized Born approximation with asymmetric descreening. *J. Chem. Theory Comput.* **5**, 2447–2464 (2009).

Author contributions

B.L. and Y.Q. conceived the original idea and designed the experiments. Q.W. and Y.Q. conducted all MD simulations and DFT calculations, as well as computational analyses. C.M.E. and B.L. collected and processed the Raman and FESEM data. C.M.E. and N.G. prepared and cycled the coin cells. X.C. prepared electrolytes and cycled the Coulombic efficiency cells. H.Z. and C.M.E. collected and processed the XPS results. Y.Z., B.L., Y.Q., E.H., X.-Q.Y. and J.L. collected and processed the SAXS–WAXS results. C.M.E., Q.W., Y.Q. and B.L. wrote the manuscript. All authors contributed to the discussions and revisions of the manuscript.

Competing interests

The authors declare no competing interests.

Additional information

Supplementary information The online version contains supplementary material available at https://doi.org/10.1038/s41563-023-01700-3.

Correspondence and requests for materials should be addressed to Yue Qi or Bin Li.

Peer review information *Nature Materials* thanks Gao Liu and the other, anonymous, reviewer(s) for their contribution to the peer review of this work.

Reprints and permissions information is available at www.nature.com/reprints.